GEOPHYSICS, VOL. 83, NO. 1 (JANUARY-FEBRUARY 2018); P. WA37–WA48, 10 FIGS., 2 TABLES.
10.1190/GEO2017-0077.1

Effect of brine-CO_2 fracture flow on velocity and electrical resistivity of naturally fractured tight sandstones

Mohammad Nooraiepour[1], Bahman Bohloli[2], Joonsang Park[2], Guillaume Sauvin[2], Elin Skurtveit[2], and Nazmul Haque Mondol[3]

ABSTRACT

Fracture networks inside geologic CO_2 storage reservoirs can serve as the primary fluid flow conduit, particularly in low-permeability formations. Although some experiments focus on the geophysical properties of brine- and CO_2-saturated rocks during matrix flow, geophysical monitoring of fracture flow when CO_2 displaces brine inside the fracture seems to be overlooked. We have conducted laboratory geophysical monitoring of fluid flow in a naturally fractured tight sandstone during brine and liquid CO_2 injection. For the experiment, the low-porosity, low-permeability, naturally fractured core sample from the Triassic De Geerdalen Formation was acquired from the Longyearbyen CO_2 storage pilot at Svalbard, Norway. Stress dependence, hysteresis, and the influence of fluid-rock interactions on fracture permeability were investigated. The results suggest that in addition to stress level and pore pressure, mobility and fluid type can affect fracture permeability during loading and unloading cycles. Moreover, the fluid-rock interaction may impact volumetric strain and consequently fracture permeability through swelling and dry out during water and CO_2 injection, respectively. Acoustic velocity and electrical resistivity were measured continuously in the axial direction and three radial levels. Geophysical monitoring of fracture flow revealed that the axial P-wave velocity and axial electrical resistivity are more sensitive to saturation change than the axial S-wave, radial P-wave, and radial resistivity measurements when CO_2 was displacing brine, and the matrix flow was negligible. The marginal decreases of acoustic velocity (maximum 1.6% for axial V_P) compared with the 11% increase in axial electrical resistivity suggest that in the case of dominant fracture flow within the fractured tight reservoirs, the use of electrical resistivity methods have a clear advantage compared with seismic methods to monitor CO_2 plume. The knowledge learned from such experiments can be useful for monitoring geologic CO_2 storage in which the primary fluid flow conduit is the fracture network.

INTRODUCTION

Carbon capture and storage (CCS) in geologic formations is a crucial near-term solution to mitigate climate change caused by atmospheric anthropogenic carbon dioxide (CO_2). Ensuring safe and secure subsurface CO_2 storage and tracking how the injected CO_2 moves within the reservoir rocks are among the key questions regarding the CCS projects (Arts and Winthaegen, 2005). In a full-scale geologic CO_2 sequestration project, millions of tons must be stored underground, the securing of which requires coupled hydraulic-geomechanical-geochemical analyses (Rutqvist, 2012). Moreover, geophysical monitoring is a necessity for establishing a reliable long-term operation (Braathen et al., 2012).

Fracture networks inside geologic CO_2 storage reservoirs can serve as the primary fluid flow conduit, particularly in low-permeability formations. The state of stress influences the fluid flow in fractures through changing the void space between the two fracture surfaces in partial contact. The initial stress field and changes in stress regimes during CO_2 injection therefore affect the hydraulic and mechanical properties of the rock mass (Pyrak-Nolte and Nolte,

Manuscript received by the Editor 31 January 2017; revised manuscript received 10 October 2017; published ahead of production 19 October 2017; published online 30 November 2017.
[1]University of Oslo (UiO), Department of Geosciences, Oslo, Norway. E-mail: mohammad.nooraiepour@geo.uio.no.
[2]Norwegian Geotechnical Institute (NGI), Oslo, Norway. E-mail: bahman.bohloli@ngi.no; joonsang.park@ngi.no; guillaume.sauvin@ngi.no; elin.skurtveit@ngi.no.
[3]University of Oslo (UiO), Department of Geosciences, Oslo, Norway and Norwegian Geotechnical Institute (NGI), Oslo, Norway. E-mail: m.n.h.mondol@geo.uio.no.

2016). Although it is the size and spatial distribution of fracture apertures that control the volumetric flow rate and hydraulic properties, it is the asperities that define the mechanical properties of fractures (Pyrak-Nolte and Nolte, 2016). The asperities are the discrete contact points between the fracture surfaces. In addition to hydraulic and mechanical properties, changes in the fluid saturation impact the geophysical responses (acoustic and electric properties) of fractured CO_2 storage reservoirs (Arts and Winthaegen, 2005).

The literature related to hydraulic and geologic aspects of fractured rocks is broad and extensive because researchers with diverse backgrounds have performed a vast range of experimental, theoretical, numerical, and field investigations (Berkowitz, 2002). Several researchers study the average fracture displacement, fracture void area, and fracture permeability as a function of applied stress (such as Pyrak-Nolte and Morris, 2000; Rogers, 2003; Huo and Benson, 2015). They report a nonlinear and inelastic behavior of fracture permeability under loading and unloading cycles. Because the fracture voids are more crack-like compared with the pores in a porous medium, the geometry of areas in contact changes more rapidly and shows higher stress sensitivity in response to the applied stresses (National Research Council, 1996). Although it is demonstrated that normal and shear stresses influence fracture permeability (National Research Council, 1996; Rogers, 2003), variations in fracture permeability at low and high stress levels and at different pore pressures for liquid and gaseous phase can be investigated further. The results would provide insights for evaluation of injectivity for different CO_2 storage candidates at different depth levels. The influence of fluid type and rock-fluid interaction (mechanical and chemical impacts) on fracture permeability for CO_2 and water should be considered too because it may alter flow pathways and consequently permeability (National Research Council, 1996; Kampman et al., 2014; Blaisonneau et al., 2016).

By considering fluid flow through matrix, several researchers conducted geophysical measurements to investigate properties of brine- and CO_2-saturated sandstones (such as Lei and Xue, 2009; Nakatsuka et al., 2010; Alemu et al., 2013; Chen et al., 2013; Nakagawa et al., 2013; Omolo, 2015; Tran, 2015; Falcon-Suarez et al., 2016a). Laboratory measurements showed that the resistivity of porous sandstones is profoundly influenced (increased to about five times) when CO_2 displaced brine in the matrix (Nakatsuka et al., 2010; Alemu et al., 2013; Omolo, 2015; Tran, 2015). Moreover, although theoretical models could estimate CO_2 saturation for clean, homogeneous rocks, they failed to provide accurate results for heterogeneous shaly reservoir rocks (Nakatsuka et al., 2010; Alemu et al., 2013). It is demonstrated that variations in porosity, matrix heterogeneity, and the layering relative to flow direction can considerably influence the CO_2 distribution pattern during drainage (Lei and Xue, 2009; Alemu et al., 2013; Nakagawa et al., 2013; Falcon-Suarez et al., 2016a). Acoustic velocity indicates a less sensitivity to fluid distribution pattern compared with resistivity (Alemu et al., 2013). During drainage of brine by CO_2, P-wave velocity V_P decreased approximately 5%–15% (Lei and Xue, 2009; Chen et al., 2013; Omolo, 2015; Tran, 2015; Falcon-Suarez et al., 2016a). Lei and Xue (2009) document that when CO_2 displaced the brine matrix saturation, an approximately 7.5%, 12%, and 14.5% decrease in V_P is expected for gaseous, liquid, and supercritical CO_2, respectively.

Despite extensive studies on the geophysical properties of brine- and CO_2-saturated rocks, there is no published research on the geophysical monitoring of CO_2 fracture flow when the contribution of the matrix flow is negligible. Lessons learned from the concurrent fluid flow and geophysical measurements on reservoir analog fractured samples can be particularly valuable for the monitoring of CO_2 plume movements during CO_2 injection in fractured reservoirs. In addition, comparing the sensitivity and detectability of acoustic and electrical resistivity techniques during dominant fracture flow provides valuable insights for geologic CO_2 storage.

This paper provides an experimental study of a naturally fractured tight sandstone core retrieved from the De Geerdalen Formation (the target CO_2 storage reservoir for the CO_2 Pilot project, Longyearbyen, Svalbard, Norway). The core sample was selected so as to have negligible matrix permeability (minimal to nonexistent matrix flow). The main research objective is geophysical monitoring (acoustic velocity and electrical resistivity) of dominant fracture flow during brine and liquid CO_2 injection. In addition, stress dependence, hysteresis, and the effect of fluid-rock interaction on fracture permeability were studied. The outcomes may provide a better understanding of the dominant fracture flow and the changes in electrical resistivity and acoustic velocity during geologic CO_2 storage.

MATERIALS AND METHODS

Reservoir and core sample properties

In the Longyearbyen CO_2 storage pilot project, it was planned to inject CO_2 into the Triassic-Jurassic tight but fractured sandstone reservoirs at a depth of 700–1000 m beneath the High Arctic community of Longyearbyen, Svalbard, Norway. The project aimed to contribute to a better understanding of CO_2 migration in the subsurface and to reduce the local anthropogenic CO_2 emissions (Braathen et al., 2012). The reservoir sandstone units at Longyearbyen are characterized with moderate secondary porosity and very low matrix permeability (Ogata et al., 2014). The in situ water injection tests documented extensive lateral fluid flow within the reservoir sandstones through the preexisting fracture networks (Ogata et al., 2014).

The naturally fractured core sample was obtained from a depth of 773.37 m in Borehole Dh2, a vertical well, 850 m deep in the Longyearbyen CO_2 storage pilot project at the Arctic Norway (Svalbard). According to the stratigraphic logs and correlation between two drilled holes Dh2 and Dh4 (Braathen et al., 2012), the selected core sample was found to be part of the Late Triassic De Geerdalen Formation. The De Geerdalen Formation represents marginal marine to lagoonal and delta plain deposits. Detailed logging of selected well within the Longyearbyen research laboratory identified a coarsening upward sandstones capped by carbonates and shales (Braathen et al., 2012). The whole-rock (bulk) mineralogical analysis of sandstone units showed that the reservoir sandstone consists mainly of quartz, feldspar, and rock fragments with minor amounts of clay, carbonate, and opaque minerals such as pyrite (Mørk, 2013). The tested sample in this study is a well-cemented sandstone (extensive quartz cement, in addition to some carbonate cement), which resulted in an extremely low matrix permeability (Table 1, <0.001 mD) and negligible matrix flow (Ogata et al., 2014). Figure 1 presents optical micrographs of extensively quartz-cemented low-porosity and low-permeability De Geerdalen sandstone. Moreover, significant porosity heterogeneity was reported in the studied sequence (Braathen et al., 2012; Magnabosco et al., 2014). As is observed in Figure 1, the thin shaly intervals and cementation caused large variations in porosity and contributed to significant heterogeneity. The sample was dry before testing. Table 1 presents properties of the tested core plug.

The identified fractures in the core samples and outcrop observations are considered as the dominant flow conduits (Ogata et al., 2014). The selected sandstone intervals in the De Geerdalen Formation show an average porosity in the range of 4%–13% and mean permeability of 0.03–0.07 mD with some local zones up to 2 mD (Farokhpoor et al., 2014). The reported values for the stiffness and tensile strength of the sandstone intervals are presented in Table 2 (Bohloli et al., 2014). The unconfined compressive strength (UCS) and tensile strength show substantial values considering the present burial depth. The observed high strength is associated with the deep burial (approximately 3.5–4.5 km) of De Geerdalen sandstones that caused chemical compaction and extensive cementation in these reservoir horizons sandstones before exhumed at present depth.

X-ray microcomputed tomography

A Nikon microcomputed tomography (CT) system (XT H 225 LC) equipped with a 225 kV microfocus X-ray tube was used for imaging the core plug before and after the tests. The spot size of the X-ray beam was approximately 3 μm, enabling a 50 μm voxel resolution. Each CT-scan consisted of 1000 2D X-ray projection images taken at different angles between 0° and 360° rotation of the sample. The projections in each scan were TIFF-formatted 16-bit images of 2000×2000 pixels. Stacks of the projection images were used to reconstruct 3D volume images with a voxel size of approximately $50 \times 50 \times 50$ μm. The 3D images were reconstructed using VGStudio MAX software (Volume Graphics Company). After reconstruction, the voxels in the 3D volume were assigned a gray value (CT number) that is proportional to the X-ray attenuation of the material. The X-ray attenuation is dependent on the density and chemical composition of the material in each voxel. Preprocessing of the reconstructed volumes consisted of correction for beam hardening and ring artifact attenuation. Subsequently, a nearest neighbor search algorithm combined with connectivity analysis was applied to estimate the fracture aperture.

Experimental setup

Two different core flooding systems were used in this study. The fluid flow system at the Norwegian Geotechnical Institute (NGI) is equipped with geophysical measurement system (ultrasonic velocity and electrical resistivity), whereas the core flooding system at the University of Oslo (UiO) is specialized for multiphase flow experiments.

Figure 2 depicts a schematic of the experimental setup at NGI. The experimental setup is designed around a fluid flow unit with an isotropic confining pressure. The confining fluid (polysiloxane fluid, SF1147 Momentive) was delivered through a computer-controlled screw pump (Global Digital Systems [GDS] pressure-volume controller). The fluid injection system consisted of two computer-controlled screw pumps (GDS pressure-volume control-

Table 1. Properties of the tested De Geerdalen sandstone core plug.

Well name	Depth (m)	Fracture type	Height (mm)	Diameter (mm)	Porosity (%)	Matrix permeability (mD)
Dh2	772.37	Natural, vertical mode I	76.03	38.26	<2.5	<0.001

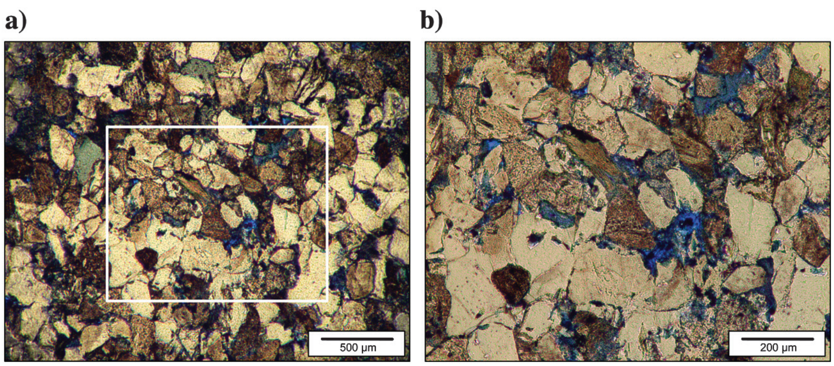

Figure 1. Micrographs of the studied De Geerdalen sandstone. (a) Optical micrograph of quartz-cemented, low-porosity low-permeability unit, the boxed region expanded in (b) quartz-cement textures such as syntaxial overgrowths on quartz grains. Light, detrital quartz with quartz-cement; darker areas, rock fragments and feldspars; blue, porosity.

Table 2. Rock mechanical properties of the De Geerdalen Formation (Bohloli et al., 2014). The experimental characterization was performed on the core plugs acquired from the Longyearbyen CO_2 storage pilot project, Svalbard, Norway.

Formation	Vertical stress (MPa)	Fracture pressure (MPa)	Density (g/cm^3)		Tensile strength, normal to bedding (MPa)		UCS (MPa)		Young's modulus (E) (MPa)	
			Average	Range	Average	Range	Average	Range	Average	Range
De Geerdalen	20.7–24.4	13	2.51	2.49–2.52	10.8	9.84–11.63	139.23	135.1–142.6	29.37	23.3–38

ler) and one dual-cylinder syringe pump (Teledyne Isco, 260D), which controlled fluid flow rate and pore pressure within the system (Figure 2). The brine (35,000 ppm NaCl salt concentration) injection was performed using the screw pump, whereas liquid CO_2 (grade 5.2, AGA Company) was injected by the syringe pump. The backpressure was controlled at the outlet using another computer-controlled GDS pressure-volume controller. Three pressure sensors monitored the fluid pressure at the inlet, outlet, and the confining volume throughout the test. The rubber sleeve, isolating the sample from the confining fluid, was equipped with sensors for geophysical measurements. As is demonstrated in Figure 3, three levels of P-wave piezo-ceramic crystals and resistivity sensors were embedded on the nitrile sleeve along the sample height that enabled us to monitor the radial P-wave velocity V_{pr} and the radial resistivity R_r. In addition, two piezoelectric transducers at the top cap and base plate were used to measure the axial P- and S-wave velocities V_{pa} and V_{sa}, and axial resistivity R_a during the experiment. Moreover, two diametrically opposed linear variable displacement transducers (LVDTs) and one radial LVDT were directly mounted on the membrane sleeve, which measured the axial and radial deformations. The LVDTs recorded the deformation with precision of 0.25–0.5 μm. The position of the radial deformation sensor is demonstrated in Figure 3a. Figure 3 also illustrates the micro-CT image of the fracture surface inside the sleeve and its relative position with respect to the three pairs of radial sensors.

The other experimental apparatus was the high-pressure high-temperature (HPHT) core flooding system (manufactured by Core Laboratories) at UiO, which was used for the measurement of the stress dependence and hysteresis of fracture permeability. It comprises a Hassler-type stainless steel core holder, two syringe pumps (inlet and outlet), back-pressure regulator, two-phase separator, and gas mass flow controllers (three different ranges). The system allows for automated management of hardware resources and data acquisition. For a detailed description of the UiO HPHT core flooding system, the reader is referred to Moghadam et al. (2016).

Permeability measurements

To measure the absolute permeability, we performed steady-state flooding tests at a constant pressure gradient condition and calculated the permeability using Darcy's law. Because the reported matrix permeability of the De Geerdalen core plug is several orders of magnitude lower than the measured permeability in this study (Braathen et al., 2012; Farokhpoor et al., 2014), the permeability values during the flooding experiments are attributed to the fracture permeability. At the pore pressure levels of the experiment, the slippage effect is highly suppressed and therefore is not considered here (Firouzi and Wilcox, 2013; Huo and Benson, 2015). All the experiments were carried out at room temperature of 19°C–21°C. Potential geochemical reactions between the rock and injected fluids considered unlikely at the experimental time scale and pressure-temperature conditions.

Ultrasonic velocity and electrical resistivity measurements

The pulse transmission technique was used to measure P- and S-wave velocities throughout the test. The technique consists of measuring the traveltime of an acoustic signal through a sample of known dimension. The ultrasonic propagation system is made up of a pulse generator, a receiver, and a digital oscilloscope for recording the signals. A resonant frequency of 500 kHz was used to generate and receive ultrasonic signals. First-arrival times were picked from the recorded waveforms using NGI's in-house software (Time Picker) and were converted to ultrasonic velocity. Details of the pulse transmission technique and velocity error analysis are presented in Nooraiepour et al. (2017). Although the sampling interval

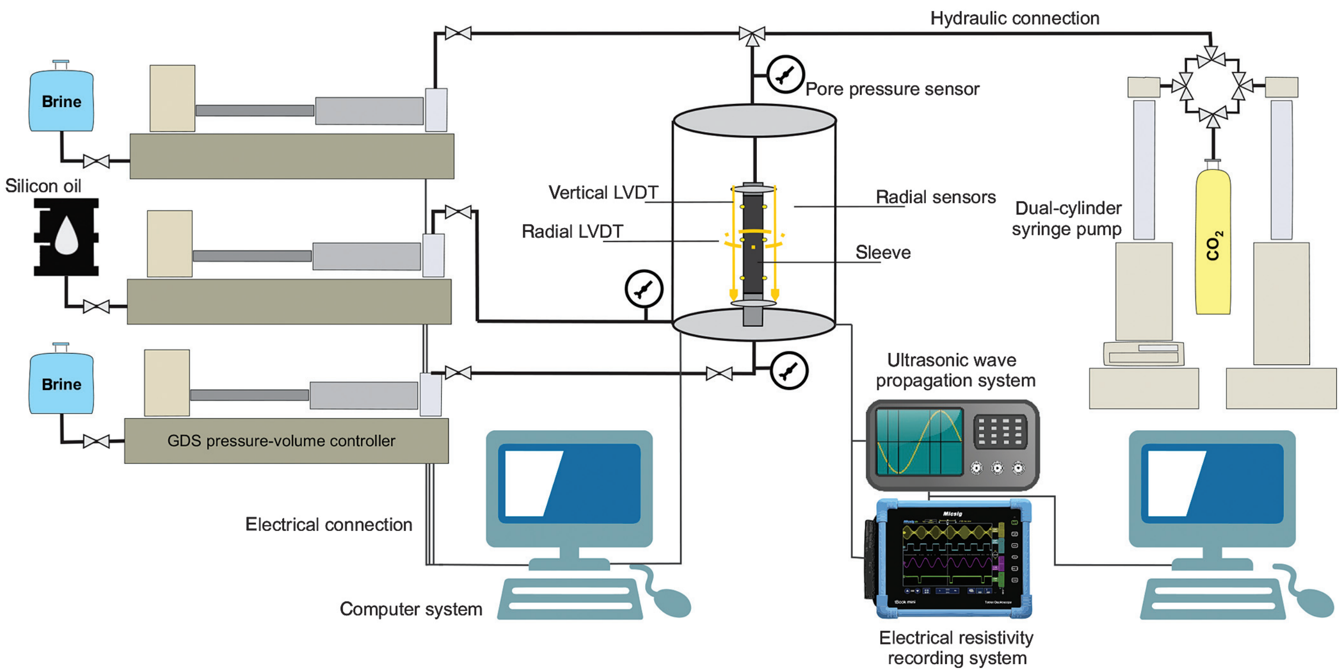

Figure 2. A schematic representation of the laboratory setup used in simultaneous fluid flow and geophysical measurements at the NGI.

for digitizing the ultrasonic waveform was the precision limiting factor (0.05 μs for axial and 0.02 μs for radial signals), the absolute error in acoustic measurements was estimated as 30 m/s for V_{pa}, 10 m/s for V_{sa}, and 20 m/s for V_{pr} (approximately 0.63%, 0.28%, and 0.43% relative error, respectively). To measure the electrical resistivity along the sample, the top cap was electrically separated from the bottom pedestal and the rest of the cell using polyether ether ketone (PEEK) tubing. The use of PEEK tubing for pore fluid flow inside the cell avoided leakage of electrical current during the measurements. In addition to the axial measurement, the resistivity was measured radially on three different levels. The electrical signal was sent through the sample by applying an input voltage of 10 V at 1 kHz frequency. For each measurement, 10 different recordings were acquired and averaged. During the experiments, the electrical resistance (ohm) was measured in the laboratory and then it was converted to electrical resistivity (ohm-m). To quantify the radial resistivity and to account for variations due to anisotropy and tortuosity, a correction factor was used to obtain the true radial resistivity. Following the procedure introduced by Wang et al. (2009) and Choi et al. (2017), numerical simulation and iteration were performed to find the correction factor.

Experimental procedures

To study stress dependence of fracture permeability, we performed flow experiments using gaseous CO_2 and deionized water (Milli-Q water). The core sample was initially considered dry and was saturated with CO_2 (after vacuuming) within the Hassler-type core holder to measure permeability to CO_2. Subsequently, after completing the CO_2 cycles, the core plug was vacuumed and dried at 60°C and then saturated with deionized water (DI-water) under vacuum for measuring liquid permeability. In these flow measurements, although the pore pressure was kept constant in each cycle (2, 3, and 4 MPa), the confining pressure was increased stepwise (3 MPa increments) up to 24 MPa. The pore pressure was calculated as the average of the fluid pressure at the inlet and the outlet. The pressure gradient across the sample was also set to be equal to the pore pressure. After finishing one loading cycle, we conducted permeability measurements during the unloading cycle. Finally, the confining pressure was completely released, and the sample was left overnight.

Although performing fluid flow using gaseous CO_2 and deionized water, we noticed a time-dependent and fluid-dependent behavior. To differentiate between the time-dependent and fluid-dependent effects and to characterize the phenomenon better, we designed and conducted a sequence of constant injection rate experiments. First, the core sample was vacuumed and dried to bring it to its original state before the experiment. Subsequently, water (deionized), CO_2 (gas), and oil (Marcol 52) were continuously flooded (1 cm^3/min) through the sample one after another, each for 48 h. The pore pressure and pressure gradient were set to be at 2 MPa. Although our study was focused on water and CO_2, we used oil (Marcol 52) to study the behavior of fracture permeability when least interaction of rock fluid or changes in volumetric strain due to the injectant was expected. The core sample was not dried nor cleaned when injection of each fluid was completed to evaluate and compare the effect of different fluids and potential rock-fluid interaction on fracture permeability.

To assess the effect of the dominant fracture flow on geophysical properties of low-porosity, low-permeability sandstones, we performed another core flooding experiment on the De Geerdalen core plug. The core sample was initially cleaned, vacuumed, and dried to bring it to its original state. The acoustic velocity and electrical resistivity were continuously recorded through the experimental phases. The test consisted of four phases: (1) Phase 1 was the consolidation and brine saturation phase, in which the confining pressure and pore pressure were simultaneously increased to 12 and 9 MPa, respectively, whereas the differential pressure was kept constant at 3 MPa; (2) flooding of brine through the fracture was carried out in the second phase, whereas the confining pressure and pore pressure was kept constant at 12 and 9 MPa, respectively; (3) in phase 3, the differential pressure (confining pressure minus pore pressure) was raised from 3 to 7.5 MPa by increasing the confining pressure to 16.5 MPa; and (4) during phase 4 (after 27,000 min), drainage core flooding was conducted by injecting liquid CO_2 and displacing brine. In phases 1–3, brine was injected from the bottom of the sample, whereas during the drainage phase (phase 4), liquid CO_2 was flooded from the top.

RESULTS

Characterization of the fracture surface

An optical image, pretest X-ray micro-CT scan of the core plug and the fracture surface are depicted in Figure 4. Moreover, pre and posttest plots of the fracture aperture are demonstrated in Figure 4d and 4e. The sample contains a vertical mode I fracture with no signs of shear movement along the fracture plane. The micro-CT image (Figure 4b) shows a heterogeneous quartz-dominated sandstone in the upper part of the sample and a siltier to shaly matrix at the bottom. The initial fracture aperture shows an open fracture with

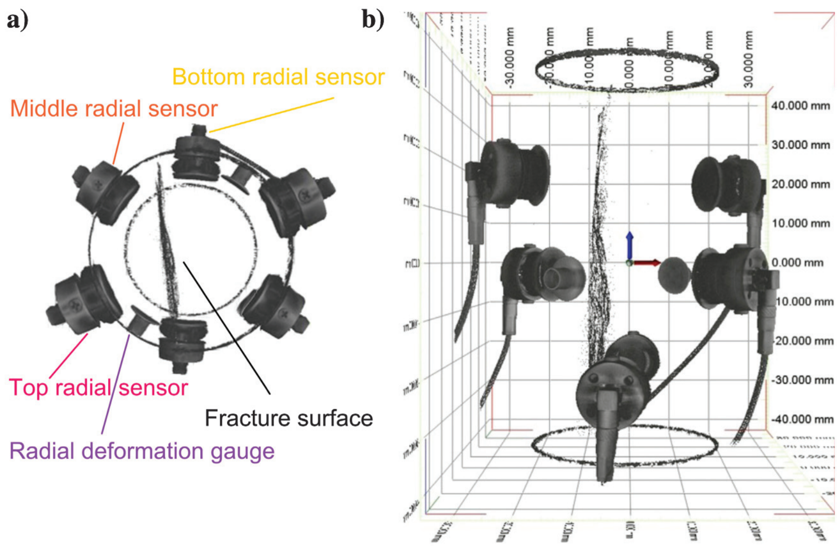

Figure 3. The relative position of three pairs of radial sensors and one radial displacement transducer with respect to the fracture surface: (a) top view and (b) side view.

a dominated aperture of approximately 150 μm, and some local contact areas and a maximum aperture of approximately 350 μm (Figure 4d). According to the classification of fractures from core and outcrop observations of the De Geerdalen Formation by Ogata et al. (2014), the tested fracture is characterized within a steep (vertical) fracture system associated with sandstone intervals and related to the last phase of tectonic uplift. This type of fracture, described as a hairline fracture in the core, often contains oxidization that indicates recent flow through the fracture. The aforementioned fracture system is considered as an important fracture type for reservoir flow in the Longyearbyen CO_2 storage pilot project.

Stress dependence and hysteresis of fracture permeability

The experimental results for fracture permeability to gaseous CO_2 and deionized water are plotted in linear scale in Figure 5a and 5b, respectively. The measured fracture permeability varies in a range from 0.1 to less than 0.01 mD (Figure 5). Although the first data points in each cycle indicate a different confining pressure due to constraints imposed by different injection pressures, the rest of the measurements reflect the same confining pressure levels (Figure 5). Figure 5 demonstrates a power law decrease of fracture permeability with the increase of confining pressure at a given pore pressure. The permeability drop is pronounced in the early loading stages. Moreover, an increase in permeability is observed with increasing pore pressure from 2 to 3 MPa and then to 4 MPa. The relative increase of fracture permeability is higher when the pore pressure increased from 3 to 4 MPa than that from 2 to 3 MPa (Figure 5). In addition, the higher the pore pressure, the lower the fracture permeability reduction during the loading cycle. When the naturally fractured sample was compressed, the fracture permeability decreased to 6%–12% of the original value at the beginning of the loading cycle. Figure 5 illustrates a gentler permeability

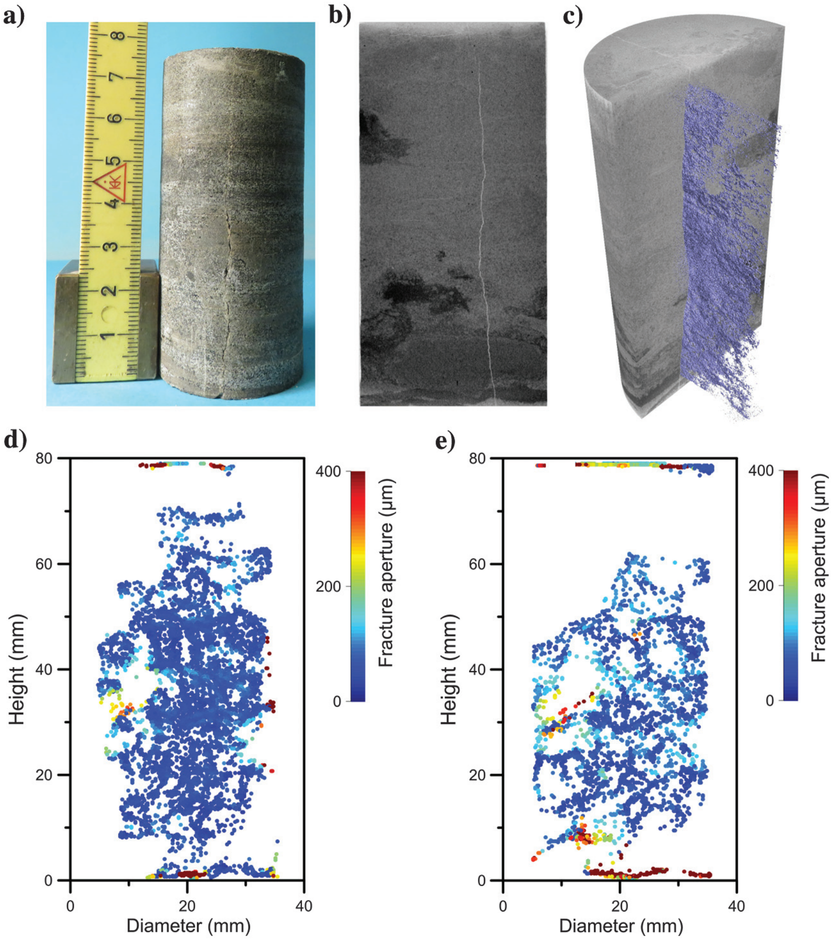

Figure 4. Illustrations of the studied naturally fractured De Geerdalen sandstone core plug. (a) Optical image, (b) micro-CT scan, and (c) fracture plane extracted from CT scanning. An interpreted fracture aperture plot of the sample (d) before and (e) after the experiment.

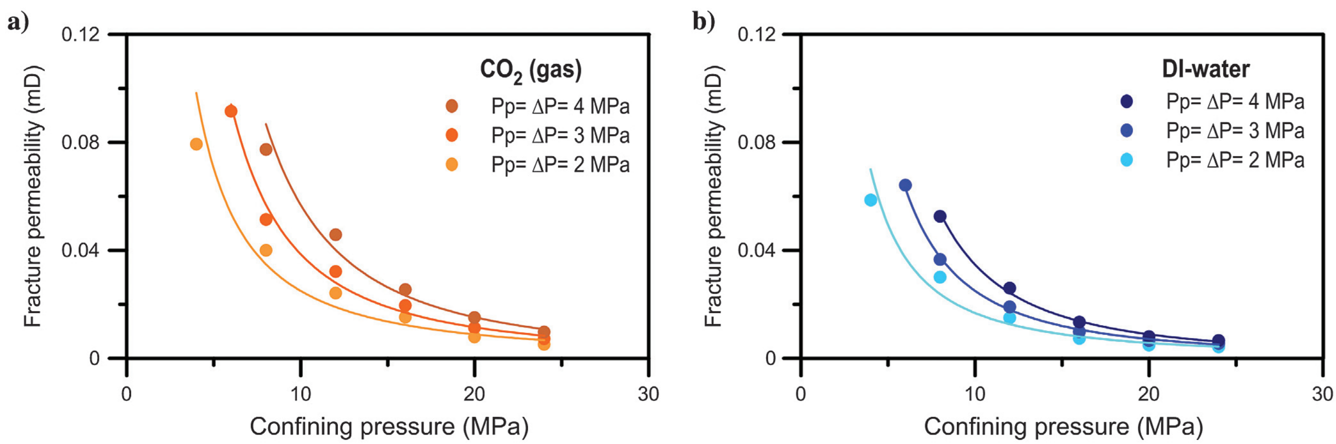

Figure 5. Stress dependence of fracture permeability. (a) Gaseous CO_2 and (b) deionized water.

reduction and higher values for gaseous CO_2 compared with DI-water. Figure 5b shows that the decrease in permeability approximately 16 MPa confining pressure is more significant for DI-water and the reductions afterward are relatively small. Moreover, for confining pressures greater than 16 MPa, the permeability to DI-water reached almost the same value for the three cycles and demonstrated less variation compared with that of gaseous CO_2 (Figure 5).

An example of hysteresis in fracture permeability is presented in Figure 6. It depicts the compression and decompression behavior of fracture permeability for gaseous CO_2 and deionized water when the pore pressure and pressure gradient across the sample was kept constant at 2 MPa. During the unloading (decompression) cycle, permeability values are consistently lower than for the loading stage (Figure 6). A semiparallel compression curve for fracture permeability is observed for gaseous CO_2 and DI-water. Throughout the decompression, permeability to the gaseous phase (CO_2) exhibits a closer trend to loading phase and indicates a lower degree of hysteresis and faster stress release compared with the liquid phase (water). When the core plug was unloaded to the initial stress level of approximately 4.5 MPa, the permeability reached 60% and 72% of its initial value for water and CO_2, respectively (Figure 6).

Time dependence and fluid effect on fracture permeability

Figure 7 shows the measured fracture permeability during the test for subsequent injection of water (deionized), CO_2 (gas), and oil (Marcol 52). The fracture permeability to water demonstrates a logarithmic reduction over time, in which 70% of the drop occurs in the first 6 h (Figure 7). Subsequent injection of gaseous CO_2 is accompanied by drying out the liquid phase and a rapid increase of permeability. The flow of oil through the sample indicates a relatively constant value during the experiment. The measured fracture permeability remained approximately constant after 48 h of injection in all three cases.

Geophysical responses during fracture flow

The results of the acoustic velocity and electrical resistivity measurements (axial and radial directions) are presented in Figure 8. The S-wave velocity was only measured in the axial direction. The axial and radial deformations are plotted in Figure 8b. Approximately 0.012 and 0.1 mm (0.031% and 0.13%) changes in diameter and height were recorded, respectively, during the experiment. Besides the major deformation in phase 1, a reduction in the height and diameter of the sample is observable during the third phase (Figure 8b). During the initial loading phase, the velocity increases almost linearly with the increase of confining pressure and pore pressure (Figure 8a and 8c). The acoustic velocity remains constant during the second phase until the beginning of phase 3 (Figure 8c). In the third phase, increasing differential pressure from 3 to 7.5 MPa while the pore pressure remained constant resulted in a 35–50 m/s (approximately 1%) increase in radial P-wave velocity V_{pr}, and an 80 m/s (1.7%) increase in axial P-wave velocity V_{pa}. The axial S-wave velocity V_{sa} demonstrates a 40 m/s (1.5%) rise throughout the third phase. As a result of the increasing differential pressure in the third phase, the V_{pa}/V_{sa} ratio shows a minute drop from 1.84 to 1.83. During liquid CO_2 injection in the fourth phase, V_{pa} and V_{pr} indicate 1.6% (80 m/s) and 0.7% (35 m/s) reduction, whereas the V_{sa} decreased approximately 0.5% (15 m/s). Consequently, V_{pa}/V_{sa} ratio decreases from 1.83 to 1.80. When looking carefully at the individual radial readings, it appears that V_{pr} reduces almost simultaneously for the three sensors. The V_{pa} and V_{pr} showed a slight increase when liquid CO_2 injection continued for next 24 h (Figure 8c).

The electrical resistivity measurements were not performed for phase 1 and a part of phase 2. Figure 8d indicates that the electrical resistivity remained almost constant during the brine injection of phase 2. After increasing differential pressure in the third phase, the axial and radial resistivity started to increase and leveled off before the end of the phase. The radial measurements follow a similar increasing trend and reflect a higher growth compared with axial one (Figure 8d). Subsequent injection of liquid CO_2 from the top caused further increase in resistivity. The measurements indicate that the resistivity increased promptly (but with different timings) in three radial levels when CO_2 injection started and remained almost constant during further injection of CO_2. The increase in electrical resistivity during drainage varies in magnitude for different sensors (approximately 3%–11%).

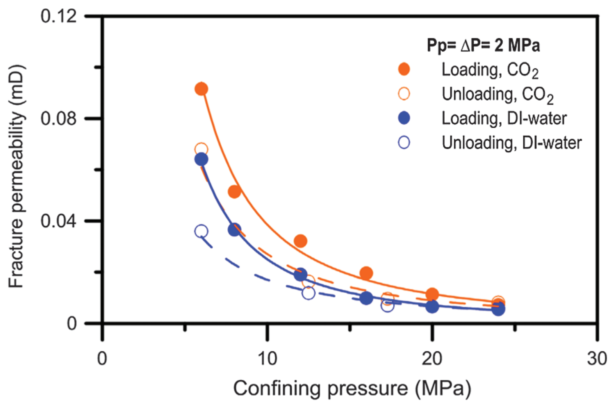

Figure 6. A plot of hysteresis in the fracture permeability for gaseous CO_2 and deionized water.

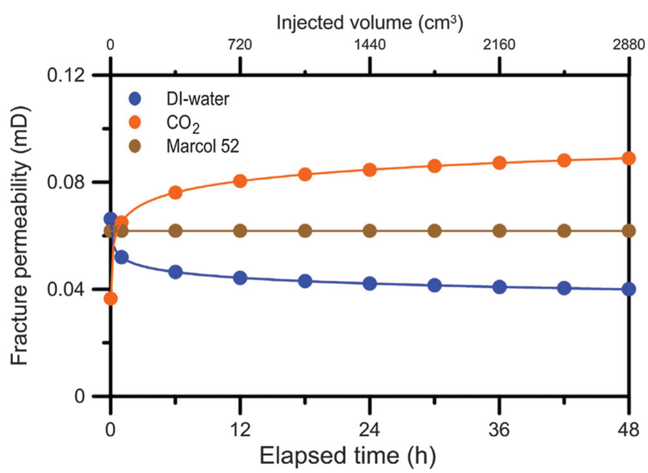

Figure 7. Influence of fluid nature on the fracture permeability observed for gaseous CO_2, deionized water, and oil (Marcol 52).

DISCUSSION

The performed permeability measurements, small changes in geophysical properties during drainage in addition to the petrographic analysis point out that the fracture is acting as preferential flow pathway in the tested core plug. In particular, measured permeabilities indicate up to two orders of magnitude higher values than the previously reported permeabilities for the matrix (Braathen et al., 2012; Farokhpoor et al., 2014). Therefore, the conducted measurements are reflecting the fracture permeability and associated changes in the geophysical properties during fracture flow.

Fluid flow investigation

Three parameters influence the fracture permeability (Zimmerman and Bodvarsson, 1996; Neuman, 2005; Sahimi, 2011): the aperture distribution, roughness, and contact area (fraction of the fracture surface with zero aperture); changes in stress influence all three. Because the reservoir units in the De Geerdalen Formation are characterized as mechanically competent rocks (Table 2), we expect that the asperities of the fracture surfaces withstand the stress field in our experiments (up to 24 MPa confining pressure). The fracture aperture distribution is heterogeneous (Figure 4), and the fracture flow is highly stress dependent (Figures 5 and 6). The increase of confining pressure (burial depth) makes the fracture smaller and more heterogeneous by reducing the mean aperture, changing the surface roughness, and broadening the variance of the aperture distribution (Huo, 2015).

The radial LVDT sensor indicated that an aperture reduction happened during the loading phases (Figure 8b). Huo and Benson (2015) document that in addition to aperture size, aperture distribution also changes during the loading and unloading cycles. First, the larger apertures get closed at early stress levels, and the contact area continues to increase while confining pressure increases (Huo and Benson, 2015). Hence, the fracture permeability reduction is pronounced at early loading steps as seen in this study. When the confining pressure is released, the aperture size can be restored gradually if the asperities did not experience severe damage during loading. Although permanent damage occurs in rock samples earlier than the maximum compressive strength (Nicksiar and Martin, 2012; Falcon-Suarez et al., 2016b), in this study, damage to asperities may not be expected on the tips of the asperities because the confining pressure levels are considerably lower than the compressive strength, larger than 135 MPa (Table 2). Because the apertures recover slowly and a portion of them remain closed, the fracture permeability values do not reach the preloading values and, as a result, show hysteresis (Figure 6). It is also demonstrated in Figure 6 that the flow of gaseous phase through the fracture causes faster recovery of apertures compared with the liquid phase, which can be associated with higher mobility and compressibility of the gaseous phase. Analysis of X-ray CT scanning revealed that hysteresis is mostly observed in the larger apertures of the fractured samples (Huo, 2015).

The experimental results in Figure 5 suggest that it is necessary to consider the stress field, pore pressure inside the fracture, and fluid type when we evaluate the fracture flow properties in a rough-

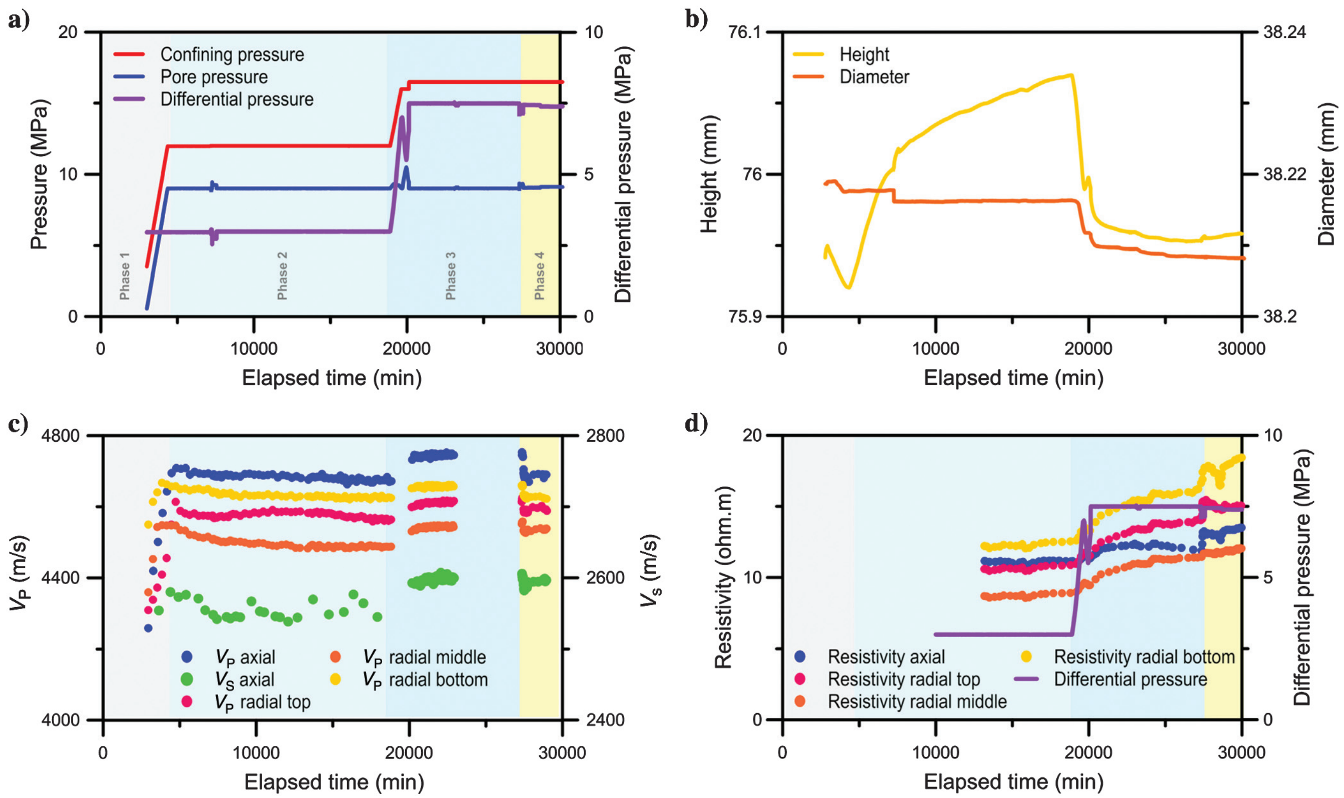

Figure 8. Simultaneous fluid flow and geophysical monitoring. (a) Four phases of the experiment, and the corresponding values for confining pressure, pore pressure, and differential pressure; (b) changes in height and diameter; (c) acoustic velocity measurements; and (d) electrical resistivity measurements.

walled fracture. It is shown for a range of confining pressures, which can also be interpreted as different depth levels, that when stress increases, fracture permeability decreases as a result of a drop in the mechanical and hydraulic aperture and a raise in the friction factor (from the modified cubic law perspective) (Witherspoon et al., 1980). However, this indicates that different pore pressure levels and fluid types (liquid and gas) can show different flow behaviors. In particular, the distinction is notable at higher stress levels (greater than 16 MPa) and in early loading stages (less than 8 MPa). In addition, Figure 6 demonstrates that in the case of pressure buildup and decompressing a single fracture, the increase in fracture permeability can be a function of stress level and fluid type. Although the changes in fracture permeability due to decompression at greater depths are small, the same range of decompression at shallower depth or for more mobile fluid (gas) can bring about higher rates of fracture flow (Figure 6).

Changes in the metastable equilibrium explain the hysteresis phenomenon (Huo and Benson, 2015). The metastability describes a dynamical system that spends an extended time in a state other than the system's least energy configuration. During the metastable configuration with a finite lifetime, all parameters that characterize the state reach and hold a fixed value. The mechanical strength of the

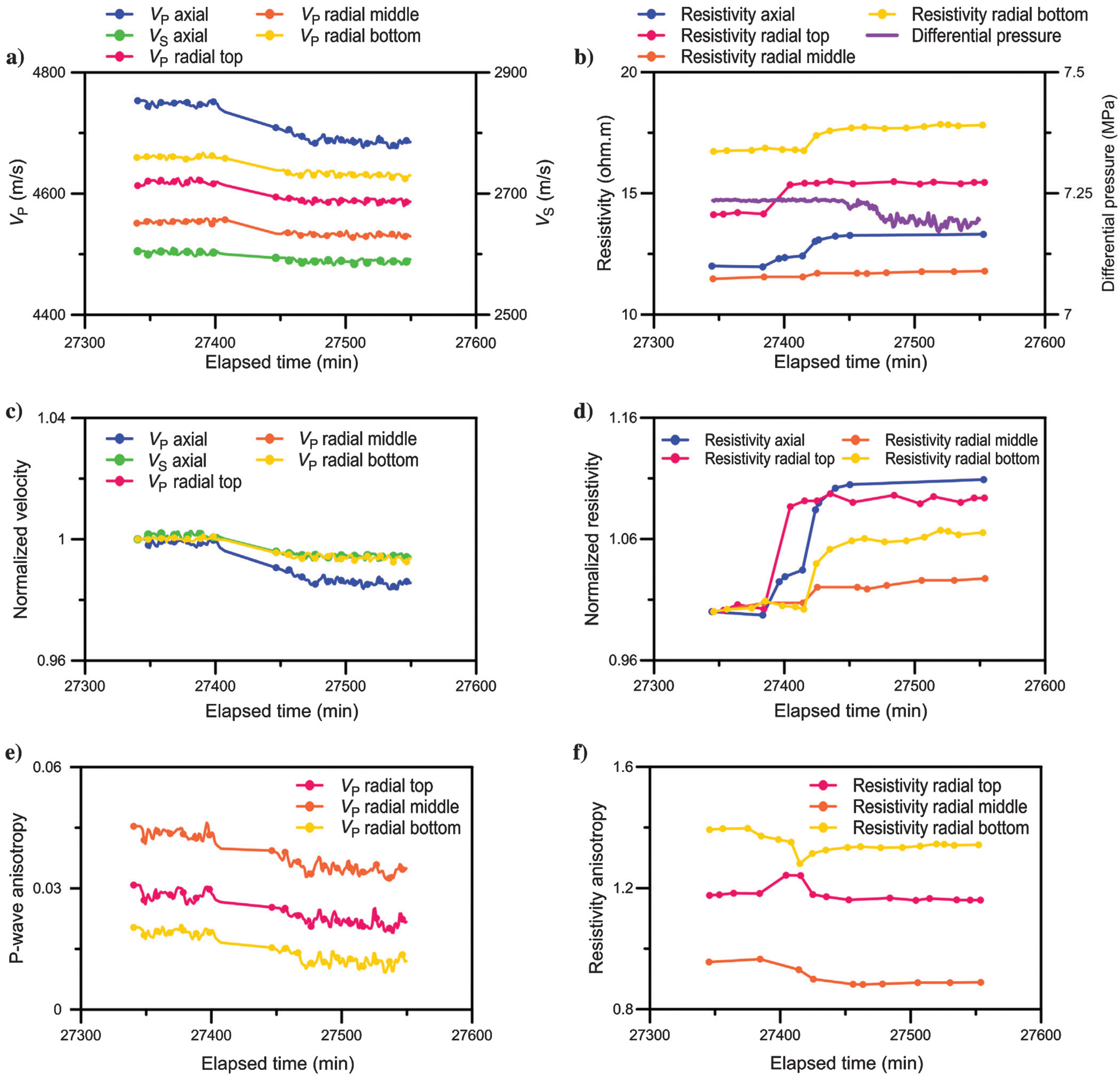

Figure 9. Changes in acoustic velocity and electrical resistivity during drainage of brine by CO_2 in the fracture. (a) Acoustic-wave velocity measurements, (b) electrical resistivity measurements, (c) normalized acoustic velocity, (d) normalized electrical resistivity, (e) P-wave anisotropy parameter, and (f) electrical resistivity anisotropy.

asperities supports the confining stress in a metastable state until the next loading breaks the equilibrium. As the confining pressure increases, the contact area increases that leads to a new metastable equilibrium. The fully elastic recovery of the fracture aperture and the extent of hysteresis depend on the mechanical strength of the rock and, in particular, asperities (Table 2). The metastable equilibrium may also explain the time-dependent behavior of fracture flow (Figure 7). During oil injection, we expected the least interaction of injectant with the core material. As a result, the fracture permeability remains constant throughout oil injection. The significant drop in fracture permeability during water injection is probably related to the matrix swelling and volumetric strain impact, which caused the relative closure and reduction of the fracture aperture. In the more plastic rocks, such as coal and organic-rich shale, matrix swelling (volumetric strain) can even result in permanent closure of fracture apertures (Mazumder and Wolf, 2008; Liu and Rutqvist, 2010). Injection of gaseous CO_2 dried the water out of the sample (Figure 7). Although the core plug was drying out during CO_2 injection, the measured fracture permeability increased logarithmically. The value of fracture permeability is almost identical for liquid phases (before swelling), whereas gaseous CO_2 shows a higher permeability (after drying out). It can be explained by the high mobility of gas compared with liquid phases when we consider the flow pathways within the thin and nonuniform fracture aperture along the fractured length (Sahimi, 2011; Kim and Moridis, 2015). Although subsequent injection of fluids could result in two-phase flow for a short period, the measured permeability in 6 h intervals for two days is considered to be single phase (or at residual wetting-phase saturation in fracture) because of the limited change in matrix saturation (the next section) and the small volume of fracture saturation. In addition, the high rate of injection (1 cm^3/min) and the elapsed time (48 h) assured single-phase flow within the fracture. The investigated sandstone horizon is also prone to long-term geochemical interactions with CO_2, which can enhance or decimate the porosity permeability through the dissolution or precipitation of calcite (Ogata et al., 2014).

Ultrasonic velocity and electrical resistivity observations

Figure 9 presents the measured and normalized values, as well as the anisotropy in the acoustic velocity and electrical resistivity during the drainage phase. Figure 9a and 9b depicts the geophysical

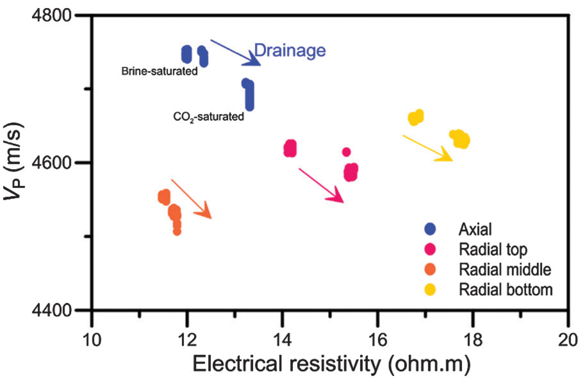

Figure 10. A cross-plot of the P-wave velocity versus electrical resistivity during the drainage phase.

measurements during the drainage at phase 4. The acoustic velocity (V_P and V_S) and electrical resistivity are normalized by the initial brine-saturated condition before injection of CO_2, and they are presented in Figure 9c and 9d, respectively. The P-wave anisotropy parameter, Thomsen's epsilon parameter (Thomsen, 1986), is depicted in Figure 9e. Epsilon measures the difference in normal stiffness between the vertical and horizontal directions (Sarout and Guéguen, 2008). The electrical resistivity anisotropy is defined as the ratio of radial (horizontal) to axial (vertical) measurements (Wang et al., 2009) and is presented in Figure 9f.

For the vertically fractured De Geerdalen core plug, Figure 9e depicts a close-to-zero Thomsen's epsilon parameter. A close-to-zero epsilon parameter refers to a relatively isotropic medium. During the drainage cycle, the P-wave anisotropy parameter decreases at all three levels as CO_2 entered the sample. The magnitude of reduction is almost the same, and a slight buildup is observed toward the end of the cycle. Likewise, Figure 9f illustrates that the anisotropy in electrical resistivity reduces upon introduction of CO_2 into the fractured core. The resistivity anisotropy then stays constant (Figure 9f). The normalized velocity measurements depict that all three V_{pr} and V_{sa} follow a close trend with a minor reduction during CO_2 injection (Figure 9c). The sensitivity of V_{pa} to CO_2 fracture flow seems higher compared with other measured velocities (Figure 9c). On the other hand, the normalized electrical resistivity curves increase abruptly with different values at each radial level (Figure 9d). Moreover, the axial resistivity measurement shows the highest increase compared with the radial readings toward the end of drainage. The sudden and small variation in acoustic velocity and electrical resistivity supports the dominant fracture flow. Comparison of radial measurements in Figure 9d illustrates that the top radial resistivity sensor detected the CO_2 flow first and the bottom one recorded the variation in resistivity last. Such variation in detecting CO_2 front or similar sensitivity to resistivity cannot be obtained from the acoustic velocity data (Figure 9c). Furthermore, the modest increase at the end of the drainage phase suggests limited saturation change within the matrix of the rock. The relative position of the radial sensors with respect to the fracture surface (Figure 3) could also contribute to the different degrees of measured anisotropy. In particular, the bottom sensor had the lowest reading angle with respect to fracture surface, whereas the top one was almost perpendicularly facing the fracture plane.

A crossplot of V_P versus electrical resistivity is presented in Figure 10. Although it is assumed that the electrical resistivity perpendicular to the bedding (vertical resistivity) is higher than the one parallel to the bedding (Wang et al., 2009), it is the radial measurements that span the whole range of the scatter (Figure 10). However, the highest V_P is recorded in the axial direction. Injection of CO_2 resulted in the movement of data points toward the bottom right, where the electrical resistivity is higher and the acoustic velocity is lower. Because the replaced brine within the De Geerdalen core plug was limited, the recorded geophysical responses show minor variations. Experimental CO_2 flooding of brine-saturated Red Wildmoor, Rothbach, and Berea sandstones (Omolo, 2015; Tran, 2015) illustrated that during matrix flow of liquid CO_2 the rate of changes in velocity and resistivity was slower and the magnitude of changes was more substantial compared with this study. Particularly, it was shown that V_P decreased 5%–15% and electrical resistivity increased three to five times (Omolo, 2015; Tran, 2015). Estimation of liquid CO_2 saturation using

Archie's equation suggests 65%–80% within the matrix of the Red Wildmoor, Rothbach, and Berea clean sandstones (Omolo, 2015; Tran, 2015), whereas the approximation for overall saturation change within the De Geerdalen sample is approximately 3%–7%.

CONCLUSION

To simulate CO_2 flow and sequestration in naturally fractured low-porosity, low-permeability sandstones, we studied a sandstone core plug of the De Geerdalen Formation in the laboratory. Our investigation of the stress dependence and hysteresis of fracture permeability indicated that at higher confining pressures (burial depth), significantly lower permeabilities (even one order of magnitude) are expected for open rough-walled fractures compared with early stress levels. Moreover, the pore pressure inside fracture and changes in the flow pathway geometry influence the fracture flow in the loading and unloading cycles. It is depicted that gaseous CO_2 may bring about a faster restoration of fracture permeability during decompression compared with the liquid phase. The impact of the fluid type on fracture permeability was found to be notable. Variations in the volumetric strain during swelling due to water injection and drying out as a result of CO_2 injection resulted in a relative decrease and increase of permeability, respectively. Injection of a noninteracting fluid (Marcol 52 oil) was recorded with steady permeability values.

Geophysical monitoring of brine-CO_2 fracture flow documented the changes in acoustic velocity and electrical resistivity when the contribution of matrix flow is negligible. The axial P-wave velocity and axial resistivity indicated the highest sensitivity to saturation change compared with the axial S-wave velocity, radial V_P, and radial resistivity when liquid CO_2 displaced brine in the fracture. A minor reduction of the P-wave anisotropy (Thomsen's epsilon parameter) is observed during CO_2 injection. Likewise, the anisotropy in electrical resistivity was reduced upon introduction of CO_2 into the fractured core. Although the front of the CO_2 flow through the fracture was detected by radial resistivity sensors, the radial V_P measurements could not record the same observation. An estimated overall 3%–7% saturation change within the De Geerdalen sample caused a 1.6% and 11% change in the axial V_P and axial electrical resistivity, respectively. The experimental results recorded a steeper change and considerably smaller variation of the geophysical responses during CO_2 fracture flow compared with previously published matrix flow measurements. The small changes of acoustic velocity suggest that the use of electrical resistivity methods is crucial for CO_2 plume monitoring when the fracture flow is dominant within the fractured tight reservoirs. It is shown that monitoring using electrical techniques may have the advantages of better detectability and higher sensitivity for geologic CO_2 storage.

ACKNOWLEDGMENTS

The authors would like to thank the Research Council of Norway funded FME-SUCCESS Centre (subsurface CO_2 storage — critical elements and superior strategies) and the University Centre in Svalbard (UNIS) CO_2 Field Laboratory for supporting the research. We appreciate UNIS for providing the core sample. The authors thank M. Soldal, L. O. Omolo, and H. Debreczeny Wilkinson for their support in performing laboratory experiments. The authors express gratitude to the associate editor and anonymous reviewers for their constructive comments and suggestions that contributed to improving this manuscript.

REFERENCES

Alemu, B. L., E. Aker, M. Soldal, Ø. Johnsen, and P. Aagaard, 2013, Effect of sub-core scale heterogeneities on acoustic and electrical properties of a reservoir rock: A CO_2 flooding experiment of brine saturated sandstone in a computed tomography scanner: Geophysical Prospecting, **61**, 235–250, doi: 10.1111/j.1365-2478.2012.01061.x.

Arts, R., and P. Winthaegen, 2005, Monitoring options for CO_2 storage, in D. Thomas, and S. M. Benson, eds., Carbon dioxide capture for storage in deep geologic formations — Results from the CO_2 capture project: Elsevier 2, 1001–1013.

Berkowitz, B., 2002, Characterizing flow and transport in fractured geological media: A review: Advances in Water Resources, **25**, 861–884, doi: 10.1016/S0309-1708(02)00042-8.

Blaisonneau, A., M. Peter-Borie, and S. Gentier, 2016, Evolution of fracture permeability with respect to fluid/rock interactions under thermohydromechanical conditions: Development of experimental reactive percolation tests: Geothermal Energy, **4**, 3, doi: 10.1186/s40517-016-0045-9.

Bohloli, B., E. Skurtveit, L. Grande, G. O. Titlestad, M. H. Børresen, Ø. Johnsen, A. Braathen, and A. Braathen, 2014, Evaluation of reservoir and cap-rock integrity for the Longyearbyen CO_2 storage pilot based on laboratory experiments and injection tests: Norsk Geologisk Tidsskrift, **94**, 171–187.

Braathen, A., K. Bælum, H. H. Christiansen, T. Dahl, O. Eiken, H. Elvebakk, F. Hansen, T. H. Hanssen, M. Jochmann, T. A. Johansen, H. Johnsen, L. Larsen, T. Lie, J. Mertes, A. Mørk, M. B. Mørk, W. Nemec, S. Olaussen, V. Oye, K. Rød, G. O. Titlestad, J. Tveranger, and K. Vagle, 2012, The Longyearbyen CO_2 Lab of Svalbard, Norway — Initial assessment of the geological conditions for CO_2 sequestration: Norwegian Journal of Geology, **92**, 353–376.

Chen, H., S. Yang, K. Huan, F. Li, W. Huang, A. Zheng, and X. Zhang, 2013, Experimental study on monitoring CO_2 sequestration by conjoint analysis of the P-wave velocity and amplitude: Environmental Science and Technology, **47**, 10071–10077, doi: 10.1021/es4017409.

Choi, J. C., L. Grande, J. Park, and N. H. Mondol, 2017, Anisotropy resistivity measurement using modified triaxial cell: Estimation of geometry factor using numerical simulation: Presented at the 4th International Workshop on Rock Physics, Trondheim, Norway.

Falcon-Suarez, I., J. Canal-Vila, J. Delgado-Martin, L. North, and A. Best, 2016b, Characterisation and multifaceted anisotropy assessment of Corvio sandstone for geological CO_2 storage studies: Geophysical Prospecting, **65**, 1293–1311, doi: 10.1111/1365-2478.12469.

Falcon-Suarez, I., L. North, K. Amalokwu, and A. Best, 2016a, Integrated geophysical and hydromechanical assessment for CO_2 storage: Shallow low permeable reservoir sandstones: Geophysical Prospecting, **64**, 828–847, doi: 10.1111/1365-2478.12396.

Farokhpoor, R., E. G. B. Lindeberg, O. Torsaeter, M. B. Mørk, and A. Mørk, 2014, Permeability and relative permeability measurements for CO_2-brine system at reservoir conditions in low permeable sandstones in Svalbard: Greenhouse Gases: Science and Technology, **4**, 36–52, doi: 10.1002/ghg.1375.

Firouzi, M., and J. Wilcox, 2013, Slippage and viscosity predictions in carbon micropores and their influence on CO_2 and CH_4 transport: Journal of Chemical Physics, **138**, 064705, doi: 10.1063/1.4790658.

Huo, D., 2015, Measuring fracture aperture and water saturation distributions using computed tomography and its application to modeling geomechanical impact on fluid flow in fractures: Ph.D. thesis, Stanford University.

Huo, D., and S. M. Benson, 2015, An experimental investigation of stress-dependent permeability and permeability hysteresis behavior in rock fractures, *in* B. Faybishenko, S. M. Benson, and J. E. Gale, eds., Fluid dynamics in complex fractured-porous systems: John Wiley & Sons Inc., 99–114.

Kampman, N., M. Bickle, M. Wigley, and B. Dubacq, 2014, Fluid flow and CO_2-fluid-mineral interactions during CO_2-storage in sedimentary basins: Chemical Geology, **369**, 22–50, doi: 10.1016/j.chemgeo.2013.11.012.

Kim, J., and G. J. Moridis, 2015, Numerical analysis of fracture propagation during hydraulic fracturing operations in shale gas systems: International Journal of Rock Mechanics and Mining Sciences, **76**, 127–137, doi: 10.1016/j.ijrmms.2015.02.013.

Lei, X., and Z. Xue, 2009, Ultrasonic velocity and attenuation during CO_2 injection into water-saturated porous sandstone: Measurements using difference seismic tomography: Physics of the Earth and Planetary Interiors, **176**, 224–234, doi: 10.1016/j.pepi.2009.06.001.

Liu, H. H., and J. Rutqvist, 2010, A new coal-permeability model: Internal swelling stress and fracture-matrix interaction: Transport in Porous Media, **82**, 157–171, doi: 10.1007/s11242-009-9442-x.

Magnabosco, C., A. Braathen, and K. Ogata, 2014, Permeability model of tight reservoir sandstones combining core-plug and miniperm analysis of drillcore; Longyearbyen CO_2 lab, Svalbard: Norwegian Journal of Geology, **94**, 189–200.

Mazumder, S., and K. H. Wolf, 2008, Differential swelling and permeability change of coal in response to CO_2 injection for ECBM: International Journal of Coal Geology, **74**, 123–138, doi: 10.1016/j.coal.2007.11.001.

Moghadam, J. N., N. H. Mondol, P. Aagaard, and H. Hellevang, 2016, Effective stress law for the permeability of clay-bearing sandstones by the Modified Clay Shell model: Greenhouse Gases: Science and Technology, **6**, 752–774, doi: 10.1002/ghg.1612.

Mørk, M. B. E., 2013, Diagenesis and quartz cement distribution of low-permeability Upper Triassic-Middle Jurassic reservoir sandstones, Longyearbyen CO_2 lab well site in Svalbard, Norway: AAPG Bulletin, **97**, 577–596, doi: 10.1306/10031211193.

Nakagawa, S., T. J. Kneafsey, T. M. Daley, B. M. Freifeld, and E. V. Rees, 2013, Laboratory seismic monitoring of supercritical CO_2 flooding in sandstone cores using the Split Hopkinson Resonant Bar technique with concurrent x-ray computed tomography imaging: Geophysical Prospecting, **61**, 254–269, doi: 10.1111/1365-2478.12027.

Nakatsuka, Y., Z. Xue, H. Garcia, and T. Matsuoka, 2010, Experimental study on CO_2 monitoring and quantification of stored CO_2 in saline formations using resistivity measurements: International Journal of Greenhouse Gas Control, **4**, 209–216, doi: 10.1016/j.ijggc.2010.01.001.

National Research Council, 1996, Rock fractures and fluid flow: Contemporary understanding and applications: National Academies Press.

Neuman, S. P., 2005, Trends, prospects and challenges in quantifying flow and transport through fractured rocks: Hydrogeology Journal, **13**, 124–147, doi: 10.1007/s10040-004-0397-2.

Nicksiar, M., and C. D. Martin, 2012, Evaluation of methods for determining crack initiation in compression tests on low-porosity rocks: Rock Mechanics and Rock Engineering, **45**, 607–617, doi: 10.1007/s00603-012-0221-6.

Nooraiepour, M., N. H. Mondol, H. Hellevang, and K. Bjørlykke, 2017, Experimental mechanical compaction of reconstituted shale and mudstone aggregates: Investigation of petrophysical and acoustic properties of SW Barents Sea cap rock sequences: Marine and Petroleum Geology, **80**, 265–292, doi: 10.1016/j.marpetgeo.2016.12.003.

Ogata, K., K. Senger, A. Braathen, J. Tveranger, and S. Olaussen, 2014, The importance of natural fractures in a tight reservoir for potential CO_2 storage: A case study of the upper Triassic-middle Jurassic Kapp Toscana Group (Spitsbergen, Arctic Norway): Geological Society Special Publication, **374**, 395–415, doi: 10.1144/SP374.9.

Omolo, L. O., 2015, Experimental study on CO_2 monitoring and saturation with combined acoustic velocity and electrical resistivity in sandstone reservoirs: Master thesis, University of Oslo.

Pyrak-Nolte, L. J., and J. P. Morris, 2000, Single fractures under normal stress: The relation between fracture specific stiffness and fluid flow: International Journal of Rock Mechanics and Mining Sciences, **37**, 245–262, doi: 10.1016/S1365-1609(99)00104-5.

Pyrak-Nolte, L. J., and D. D. Nolte, 2016, Approaching a universal scaling relationship between fracture stiffness and fluid flow: Nature Communications, **7**, 10663, doi: 10.1038/ncomms10663.

Rogers, S. F., 2003, Critical stress-related permeability in fractured rocks: Geological Society Special Publication, **209**, 7–16, doi: 10.1144/GSL.SP.2003.209.01.02.

Rutqvist, J., 2012, The geomechanics of CO_2 Storage in deep sedimentary formations: Geotechnical and Geological Engineering, **30**, 525–551, doi: 10.1007/s10706-011-9491-0.

Sahimi, M., 2011, Flow and transport in porous media and fractured rock: From classical methods to modern approaches, 2nd ed.: Wiley.

Sarout, J., and Y. Guéguen, 2008, Anisotropy of elastic wave velocities in deformed shales: Part 1. Experimental results: Geophysics, **73**, no. 5, D75–D89, doi: 10.1190/1.2952744.

Thomsen, L., 1986, Weak elastic anisotropy: Geophysics, **51**, 1954–1966, doi: 10.1190/1.1442051.

Tran, T. X., 2015, Monitoring CO_2 behaviour during injection into reservoir sandstone: Master thesis, University of Oslo.

Wang, Z., L.-J. Gelius, and F.-N. Kong, 2009, Simultaneous core sample measurements of elastic properties and resistivity at reservoir conditions employing a modified triaxial cell — A feasibility study: Geophysical Prospecting, **57**, 1009–1026, doi: 10.1111/j.1365-2478.2009.00792.x.

Witherspoon, P. A., J. S. Y. Wang, K. Iwai, and J. E. Gale, 1980, Validity of cubic law for fluid-flow in a deformable rock fracture: Water Resources Research, **16**, 1016–1024, doi: 10.1029/WR016i006p01016.

Zimmerman, R. W., and G. S. Bodvarsson, 1996, Hydraulic conductivity of rock fractures: Transport in Porous Media, **23**, 1–30, doi: 10.1007/BF00145263.